AFRL-RX-WP-TP-2011-4115

TECHNIQUE FOR AUTOMATED EXTRACTION OF SYMMETRIC MICROSTRUCTURAL FEATURES:APPLICATION TO DENDRITIC CORES IN SINGLE CRYSTAL NI-BASED SUPERALLOYS

M.A. Tschopp, M.A. Groeber, J.P. Simmons, A.H. Rosenberger, and C. Woodward

Metals Branch
Metals, Ceramics & Nondestructive Evaluation Division

MARCH 2011

AIR FORCE RESEARCH LABORATORY
MATERIALS AND MANUFACTURING DIRECTORATE
WRIGHT-PATTERSON AIR FORCE BASE, OH 45433-7750
AIR FORCE MATERIEL COMMAND
UNITED STATES AIR FORCE

REPORT DOCUMENTATION PAGE

Form Approved
OMB No. 0704-0188

1. REPORT DATE *(DD-MM-YY)*	2. REPORT TYPE	3. DATES COVERED *(From - To)*
March 2011	Journal Article PREPRINT	14 June 2010 – 14 June 2010

4. TITLE AND SUBTITLE
TECHNIQUE FOR AUTOMATED EXTRACTION OF SYMMETRIC MICROSTRUCTURAL FEATURES:APPLICATION TO DENDRITIC CORES IN SINGLE CRYSTAL NI-BASED SUPERALLOYS (PREPRINT)

5a. CONTRACT NUMBER
In-house

5b. GRANT NUMBER

5c. PROGRAM ELEMENT NUMBER
62102F

6. AUTHOR(S)
M.A. Tschopp, M.A. Groeber, J.P. Simmons, A.H. Rosenberger, and C. Woodward

5d. PROJECT NUMBER
4347

5e. TASK NUMBER
20

5f. WORK UNIT NUMBER
LM121100

7. PERFORMING ORGANIZATION NAME(S) AND ADDRESS(ES)
Metals Branch (AFRL/RXLM)
Metals, Ceramics & Nondestructive Evaluation Division
Materials and Manufacturing Directorate
Wright-Patterson Air Force Base, OH 45433-7750
Air Force Materiel Command, United States Air Force

8. PERFORMING ORGANIZATION REPORT NUMBER
AFRL-RX-WP-TP-2011-4115

9. SPONSORING/MONITORING AGENCY NAME(S) AND ADDRESS(ES)
Air Force Research Laboratory
Materials and Manufacturing Directorate
Wright-Patterson Air Force Base, OH 45433-7750
Air Force Materiel Command
United States Air Force

10. SPONSORING/MONITORING AGENCY ACRONYM(S)
AFRL/RXLM

11. SPONSORING/MONITORING AGENCY REPORT NUMBER(S)
AFRL-RX-WP-TP-2011-4115

12. DISTRIBUTION/AVAILABILITY STATEMENT
Approved for public release; distribution unlimited.

13. SUPPLEMENTARY NOTES
Journal article was submitted to Scripta Materialia Journal.
This is a work of the U.S. Government and is not subject to copyright protection in the United States. Technical paper contains color.
PAO Case Number and clearance date: 88ABW-2010-3436, 22 Jun 2010.

14. ABSTRACT
Serial sectioning methods continue to produce a wealth of image data for quantifying the three-dimensional nature of material microstructures. In this work, we discuss a computational methodology for automated detection and 3D characterization of dendrite cores from images taken from slices of a production turbine blade made of a heat-treated single crystal Ni-based superalloy. The dendrite core locations are detected using an automated segmentation technique that incorporates information over multiple length scales and exploits the four-fold symmetry of the dendrites when viewed down the {100} growth direction. Additional rules that take advantage of the continuity of the dendrites from slice to slice help to exclude segmentation artifacts and improve dendrite core segmentation. The significance of this technique is that it may be extended to include any symmetric features.

15. SUBJECT TERMS
single crystal; nickel-based superalloy; characterization; dendrite core; feature extraction; image processing

16. SECURITY CLASSIFICATION OF:			17. LIMITATION OF ABSTRACT:	18. NUMBER OF PAGES	19a. NAME OF RESPONSIBLE PERSON (Monitor)
a. REPORT	b. ABSTRACT	c. THIS PAGE			Andrew Rosenberger
Unclassified	Unclassified	Unclassified	SAR	24	19b. TELEPHONE NUMBER *(Include Area Code)* N/A

Technique for Automated Extraction of Symmetric Microstructural Features: Application to Dendritic Cores in Single Crystal Ni-Based Superalloys

M.A. Tschopp[a,*], M.A. Groeber[b], J.P. Simmons[b], A.H. Rosenberger[b], C. Woodward[b]

[a] *Center for Advanced Vehicular Systems, Mississippi State University, Mississippi State, MS 39762*

[b] *Air Force Research Laboratory, Materials and Manufacturing Directorate, AFRL/RX Wright Patterson AFB, OH 45433*

Abstract

Serial sectioning methods continue to produce a wealth of image data for quantifying the three-dimensional nature of material microstructures. In this work, we discuss a computational methodology for automated detection and 3D characterization of dendrite cores from images taken from slices of a production turbine blade made of a heat-treated single crystal Ni-based superalloy. The dendrite core locations are detected using an automated segmentation technique that incorporates information over multiple length scales and exploits the four-fold symmetry of the dendrites when viewed down the$\langle 100 \rangle$ growth direction. Additional rules that take advantage of the continuity of the dendrites from slice to slice help to exclude segmentation artifacts and improve dendrite core segmentation. The significance of this technique is that it may be extended to include any symmetric features.

Keywords:
single crystal; nickel-based superalloy; characterization; dendrite core; feature extraction; image processing

1. Introduction

Knowledge of the three-dimensional (3D) nature of microstructural features is important for ascertaining certain properties in many material systems. While a variety of two-dimensional (2D) techniques (e.g., conventional optical microscopy, scanning electron microscopy, transmission electron microscopy, and electron backscatter diffraction) exist for determining microstructure morphology, interconnectivity, crystallography grain orientations and grain boundary character on

*Corresponding Author
Email address: mtschopp@cavs.msstate.edu (M.A. Tschopp)

surfaces, these conventional 2D techniques are often inadequate for accurately determining the true 3D nature of microstructure features in most materials of even moderate microstructural complexity. Hence, serial sectioning is a labor-intensive, but effective, tool that is often used to provide datasets essential for characterizing the three-dimensional (3D) microstructure in many material systems. The ability to automate the removal of material at controlled rates through either mechanical polishing [1-3], microtome milling, or focused ion beam milling [4-8], has enabled researchers to obtain 3D microstructure datasets at a range of length scales. To further enhance the speed of collecting these datasets, the method of removal is often coupled with the imaging instrument, e.g., mechanical polishing with optical imaging [1], or FIB with EBSD imaging [4-7]. This technique has helped to produce the 3D microstructure in a number of materials: the polycrystalline grain structure in Ni-based superalloys (IN100) [5], the dendritic structure in single crystal nickel-based superalloys [9, 10], Al-Cu alloys [11, 12], and Pb-Sn alloys [13, 14], the reinforcement particle for particle-reinforced metal-matrix composites [15, 16], microstructure (cementite, ferrite, austenite, martensite, and pearlite) colonies in alloy steels [17-20], the structure of pitch-based carbon foams [21], the γ-$\gamma\prime$ microstructure in Ni alloys [4, 22, 23], the intermetallic particles in Sn-rich solder [24], and the pore morphology in die-cast magnesium alloys [25], to name a few.

In this work, the 3D dendritic microstructure in single crystal nickel-based superalloys is investigated. Large montage images from the airfoil section of a turbine blade were used to obtain the 3D dendritic structure. In single crystal nickel-based superalloys, the dendritic structure is the most striking feature of the microstructure as this is the first region to solidify. In addition to providing insight into its growth within the turbine blade, the 3D dendritic structure may also provide insight into the occurrence and spatial relationship of pores and eutectic particles, which may be important to consider for fatigue simulations. Parallel work concentrates on automated detection and 3D characterization of eutectic particles to reconstruct the interdendritic structure of the blade [26]. Identifying both of these features is important for obtaining a quantitative description of the structure of single crystal nickel-based superalloys used in turbine blade applications.

Successful efforts to automate serial sectioning techniques to produce large sets of microstructure images [1, 2, 9, 10] have led to overwhelming amounts of data resulting in a bottleneck at the image processing and analysis step. This statement is particularly true for the image segmentation step in complex multi-component microstructures, e.g., the eutectic particles, pores, carbides, and dendrites in the single crystal microstructure investigated here. While manual identification of dendrites in single crystal nickel-based superalloys can be done for tens to a few hundred dendrites, this process is very time-consuming for larger numbers of dendrites. Typical data sets can contain 50 or more serial slices with at least 250 dendrite cores per slice, so the time required to manually identify these features is substantial. Automating the identification and reconstruction of microstructural features will be required for this approach to reach its full

potential. Reliable assessment of microstructural statistics will require processing large datasets.

The rapid growth in 3D microstructure characterization is driven by the requirements of integrated computational models that link processing to structure to properties and performance. From a properties perspective, 3D microstructure statistics can enhance the predictive capability of finite element models that take microstructure into account. Reconstructing the microstructure at the relevant length scale(s) for high temperature mechanical behavior can be used in concurrent multi-scale FE models that account for material microstructure. For instance, Ghosh and coworkers [27] have developed a concurrent multi-level model whereby multiple levels of refinement are used to simulate crack growth behavior. The level zero continuum approximation corresponds to a constitutive response consistent with a homogenization of microstructure and properties over the entire domain of the turbine blade. Level one would capture the variation in response produced by crystal rotations of different dendritic domains, and the density of primary dendrites (primary dendrite arm spacing). Finer details in the microstructure such as the secondary arm spacing, eutectic phase, carbide and void distribution would be captured in a level two representation. One objective of this research is to measure the statistics necessary to generate statistically representative volume elements for inclusion in these models.

The present article discusses an automated image processing technique for extracting symmetric features in microstructural images. In materials science applications, symmetry often plays a role in the development of microstructure (especially in crystallography), yet symmetry is seldom used for image processing techniques. Subsequently, this technique is applied to a single crystal nickel-based superalloy to identify dendrite core locations by using their four-fold symmetry as viewed along the $\langle 100 \rangle$ growth direction. A previous short communication by the present authors [28] applies this symmetry-based technique to a single image for this application, without discussing the details of how to account for confounding features in the microstructure or how to incorporate information from adjacent slices. The key results of this study are how to extract the locations of symmetric microstructural features in images by using the symmetry-based technique [28] augmented with information from adjacent slices and confounding image features (e.g., microstructure, eutectic particles).

This paper is outlined as follows. Section 2 briefly discusses the acquired serial images and describes the difficulties encountered with extracting dendrite core locations from these images. Section 3 describes the automated symmetry-based technique and its application to images that contain both microstructure and mount material (Section 3.1 and 3.2), its use of slice continuity for improved segmentation (Section 3.3), and its current problems and potential areas of improvements (section 3.4). The significance of this technique is that it can be extended to include any symmetry features such as mirror planes, improper rotations, or color symmetry, by using suitable matrix representations of these operations. For simplicity, only the four-fold rotation is included in this work.

2. Image Acquisition

Figure 1 shows an etched optical image montage for a serial slice perpendicular to the nominal growth direction of a single crystal nickel-based superalloy (PWA 1484) turbine blade, which was fillet cut through the interior passage. Further details of the experimental method for obtaining the images are given in Groeber et al. [29]. The green (small) box is an image showing a single dendrite as viewed from the ⟨100⟩ growth direction and is used for describing the algorithm in Figure 2. The blue (intermediate) box is an image of a group of dendrites along with eutectic particles (bright particles within the interdendritic area), which is used to assess the symmetry-based technique (Figure 3). Last, the red (large) box delineates a 6-mm x 6-mm (3000 x 3000 pixels) subset of the turbine blade that is subsequently used to test the technique on a microstructural area with a large number of features that can bias the calculation (i.e., both the mount material and eutectic particles).

There are several problems associated with manual or standard image processing methods to identify dendrite cores.

1. **Large amount of image information.** The large size of the images and the potential number of slices required to reconstruct the dendritic structure for a large amount of material make it difficult to manually identify the dendrite cores in each slice. For instance, the pixel spacing for the optical images is approximately 2-μm and the image size shown in Figure 1 is 35 mm x 8 mm (17544 x 4244 pixels). The number of dendrite cores manually identified routinely approaches 500 or more in some slices.
2. **Intensity changes within image.** The etchant used to highlight dendrite cores can etch material at different rates within the same slice, varying the contrast in intensity for the dendrite cores and arms. Additionally,

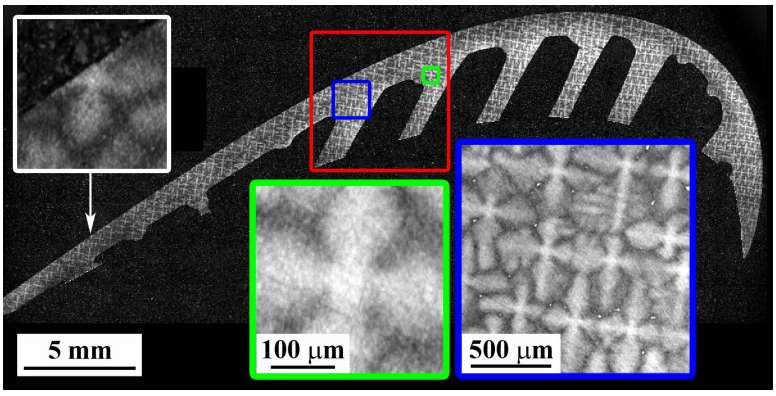

Figure 1: This image montage shows the microstructure of a cross-section of a single crystal nickel-based superalloy turbine blade [28]. The red, blue, and green boxes highlight microstructural areas used for the symmetry-based technique.

each montage image is the result of stitching multiple individual images together. Occasionally, an individual image may be out-of-focus or the image contrast may change slightly in the region where two individual images were stitched together. Standard methods for leveling the contrast within the blade region to correct this do not account for the mount material, which would incorrectly skew intensity values near the edges of the blade.

3. **3D dendrite morphology.** The 2D shape of the 3D dendrite structure is continually changing on successive images. Additionally, the dendrite arms within a serial slice may not all be similarly oriented, i.e., there may be a range of dendrite arm orientation angles with respect their respective dendrite cores. Both of these can be problematic for cross correlation techniques [30, 31], which typically use a template (a particular object or region, e.g., a typical dendrite shape in this case) to determine the locations of similar features within a larger image.

Therefore, a technique other than manual identification is required for processing these large images. To address these problems, the automated symmetry-based technique presented in Section 3 is almost entirely automated, requiring very little operator intervention. Also, this technique uses image information from the local region around each pixel to offset any potential intensity contrast over the serial montage image due to the image acquisition process. Moreover, by using the four-fold symmetry of the dendrite arms as viewed from the $\langle 100 \rangle$ growth direction, the problematic element of the potential variability in the dendrite arm orientations for cross correlation techniques is eliminated.

3. Four-fold Symmetry Filter

3.1. Methodology and Application to Simple Image

Conventional image processing uses only the intensity information in the image, which is conventionally known as "observation information." This work builds on conventional methods by including the "prior information" that the cores should, on average, have four-fold symmetry, when viewed along the $\langle 100 \rangle$ growth direction (i.e., see the green box in Figure 1). The observation information would be the differences in intensity and textures for the different constituents of the image: the mount material, the dendrites, the eutectic particles and the interdendritic region. Combining this observation information with the prior information of the symmetry allows automatic identification of the cores.

By calculating a quantitative symmetry parameter for each pixel in an intensity image, those pixels in local neighborhoods with a high four-fold symmetry parameter can be detected using a simple threshold. Figure 2 shows a schematic of how the symmetry parameter is evaluated for a single pixel without accounting for mount material or eutectic particles. The red (large) image from Figure 1 is shown in Figure 2(a). The four-fold symmetry parameter for a single pixel within this image is calculated as follows:

1. A single pixel within Figure 2(a) is chosen to calculate the four-fold symmetry parameter. Then, a local neighborhood around the pixel is identified for a particular length scale (e.g., 300-μm x 300-μm in Figure 2) and the associated intensity image of this neighborhood is used for the four-fold symmetry filter (Figure 2(b)).
2. The intensity image (Figure 2(b)) is subsequently rotated by 90° three times to produce the images shown in Figures 2(c)-2(e).
3. A local average intensity image (Figure 2(f)) is calculated from the four rotated images in Figures 2(b)-2(e). When there are features within the local neighborhood that should not be taken into account for the four-fold symmetry parameter, the average intensity image may need to be corrected. Figure 2(g) is the result after accounting for these features (no effect in this example). How this technique accounts for these features is shown in Figure 5 and discussed in Section 3.2.
4. Figure 2(h) shows an image of the deviation at every pixel between the intensity values in Figure 2(g) and Figure 2(b). The l^2-norm (square root of the sum of the squares of the pixels) is inverted to calculate the scalar symmetry parameter of the local neighborhood for the single starting pixel (0.051).

To test the applicability of the four-fold symmetry filter to extracting dendrite core locations, the 1.4-mm x 1.4-mm blue (intermediate) image was selected from the serial slice. Three different neighborhood sizes were used to investigate the influence of neighborhood size on the results: 100, 200 and 300 μm. Figure 3 shows the resulting images for the four-fold symmetry filter using neighborhood sizes of 100 μm (a), 200 μm (b), and 300 μm (c). Visual comparison of the dendrite core locations in the original image (Figure 1, blue) with the four-fold filtered images shows that the intensity is high in the dendrite core locations. However, the intensity is also often high in the secondary arms and sometimes in the interdendritic area, so a simple threshold at any length scale may be inadequate for segmenting the dendrite core locations from these filtered images. The original intensity information can also be useful for detecting the correct symmetric features (e.g., distinguishing four-fold symmetric dendritic regions from four-fold symmetric interdendritic regions). Also, notice that the eutectic particles in Figures 3(a)-3(c) are shown in black. This does not reflect an absence of four-fold symmetry in these particles; rather, the eutectic particles were previously segmented using an automated region growing technique [26, 32] and are accounted for in the four-fold symmetry filter so they do not affect the extraction of the dendrite core locations.

The technique was made more robust by segmenting the dendrite core locations with a vector-based segmentation approach using the four-fold symmetry parameters. In this manner, each pixel within the original image has a vector associated with it that reflects information from multiple length scales. For example, in this case, the four-fold symmetry parameters for local neighborhood sizes of 100, 150, 200, 250, and 300 μm were used to construct a vector-based image to help segment the dendrite cores. Then, the dimensionality of this

vector-based image is reduced by taking the l^2-norm of the vector within each pixel and multiplying by the original intensity image (to further reduce peaks in secondary/tertiary dendrite arms and interdendritic areas). Again, the intensity information of the original image is used to differentiate four-fold symmetry in the dendrite cores from that in the interdendritic regions.

Additionally, weighting the four-fold symmetry parameter at different length scales using the corresponding standard deviation of the local neighborhood intensities is important for smaller length scales where high four-fold symmetry parameters may reflect that the homogeneity of intensities within a local neighborhood rather than the actual four-fold symmetry (e.g., the local region lies entirely within a dendrite arm). Figures 3(d)-3(f) show the weighting factors for the corresponding images in Figures 3(a)-3(c), using the standard deviations from neighborhood sizes of 100 μm, 200 μm, and 300 μm, respectively. The values on the scale marker on the right-hand side of Figure 3(f) reflect the five different neighborhood sizes. The weighting factor for each pixel at each scale is simply the standard deviation for intensities within that neighborhood divided by the sum of standard deviations over all scales for that pixel. Notice that some of the high four-fold symmetry values in the 100 μm image (Figure 3(a)) have a

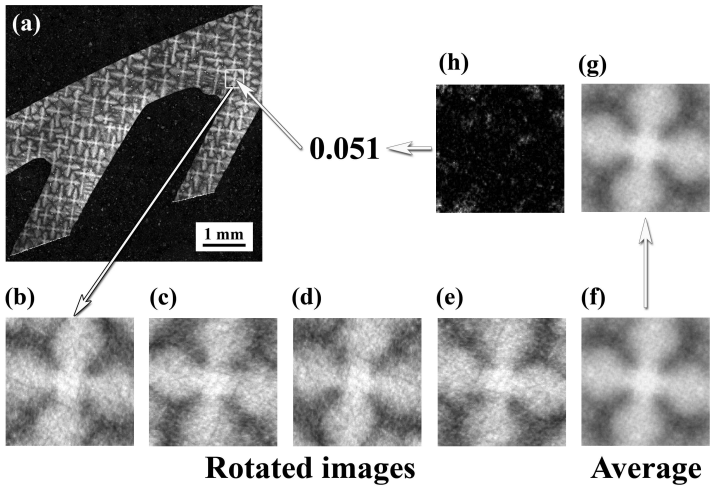

Figure 2: This schematic shows how a single pixel within the image is processed using the four-fold symmetry filter [28]. A 300-μm x 300-μm local image (b) surrounding a single pixel within (a) is chosen and rotated in 90° increments to produce (c)-(e). Image (f) is the average of the four rotated images and (g) is the corrected average for the mount material and eutectic particles (not required here). Image (h) shows the deviation between image (g) and image (b). The inverse of the sum of the values in image (h) is the four-fold symmetry parameter for the starting pixel.

low weighting factor (0.05) in Figure 3(d), whereas the weighting factor would be 0.20 if all scales were weighted evenly. This desensitizes the vector-based image to high four-fold symmetry values due to similar intensities over a local neighborhood on a per pixel basis.

Figure 4 shows images from the vector-based segmentation. Figure 4(a) shows the single output image generated by combining the four-fold symmetry images with the weight factor images at the five neighborhood sizes. While many of the dendrite cores have high four-fold symmetry values, some interdendritic areas also have high four-fold symmetry values. Figure 4(b) multiplies Figure 4(a) by the original intensity image. If the background intensity changes significantly, the original intensity image may need to be leveled before this operation. Figure 4(c) shows the image after applying further image processing operations to help accentuate the peaks for detection. First, Gaussian smoothing is used to reduce noise within the image. Then, a morphological top hat filter is applied to enhance the peak definition.

The resulting image from the multi-scale four-fold symmetry filter (Figure 4(c)) can now be segmented to extract the dendrite core locations. Prior to this point, the four-fold symmetry filters can operate in an automated fashion requiring no user intervention. While various automated segmentation methods exist [e.g., 33-34], this image is easily segmented using a user-defined threshold

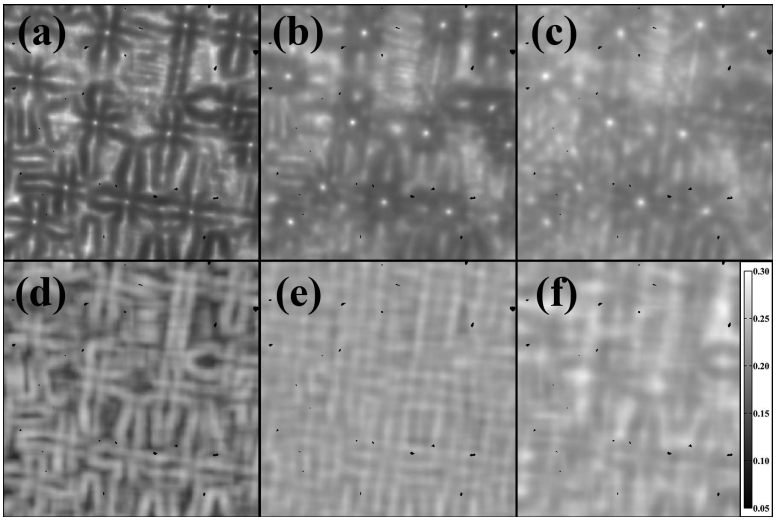

Figure 3: The four-fold symmetry filter was applied to the original intensity image (shown in blue in Figure 1). The resulting values from the symmetry filter are rescaled to form 8-bit images and are shown in (a), (b), and (c) using neighborhood sizes of n = 100 μm, 200 μm, and 300 μm, respectively. The corresponding weighting factor images for (a), (b), and (c) are shown in (d), (e), and (f), respectively.

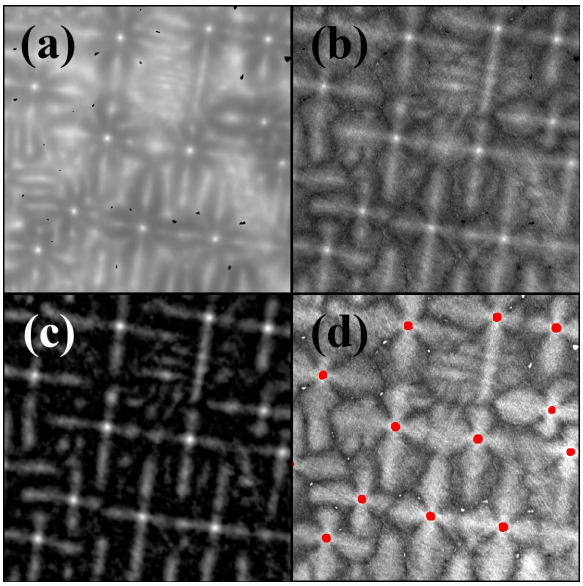

Figure 4: Image (a) was obtained using the four-fold symmetry and weighting factor images at five length scales (e.g., see the images in Figure 3). After multiplying by the original intensity image (b), a further Gaussian and top hat operation are applied to produce the vector-based final image (c). A user-specified threshold parameter was applied to (c) and the segmented dendrite cores (red) are superimposed onto the original intensity image (d).

parameter. In this image, the range of user-defined intensity thresholds that correctly identified all dendrite core locations was quite large (range of 141-202 when this image was rescaled to an 8-bit image). Figure 4(d) superimposes the segmented dendrite core locations (in red) obtained using a threshold parameter of 142 onto the original intensity image. This technique identified all the dendrite cores while only requiring the manual manipulation of a single parameter (the threshold parameter).

3.2. Application to Complex Image with Edge Effects

Extending the four-fold symmetry filter to the large image in Figure 1 requires dealing with edge effects due to the mount material, though. For instance, in local neighborhoods that contain the mount material, the four-fold symmetry would be extremely low for a dendrite core near the boundary. Therefore, the mount material needs to be accounted for in the symmetry filter. Moreover, the eutectic particles can decrease the four-fold symmetry value in a similar way to the mount material. In prior work [26], the mount material and eutectic particles were segmented for 16 successive serial images that were spaced approximately 10 μm apart. As an example of how the four-fold symmetry filter is modified to account for edge effects, this same set of 6 x 6-mm images is used in this article.

Figure 5 shows a schematic of how a single pixel within the image is processed using the four-fold symmetry filter at a single length scale (300 x 300 μm). This schematic is similar to that in Figure 2, except that the mount material and eutectic particles are included in this region. The four-fold symmetry value for a single pixel within this image is calculated as follows:

1. A single pixel within Figure 5(a) is chosen and then a 300 x 300-μm intensity image centered about the pixel is used for the four-fold symmetry filter (Figure 5(b)). A complementary 300 x 300-μm binary image for Figure 5(b) that indicates pixels belonging to the mount material and eutectic particles (in black) is also shown in Figure 5(g). Additionally, the

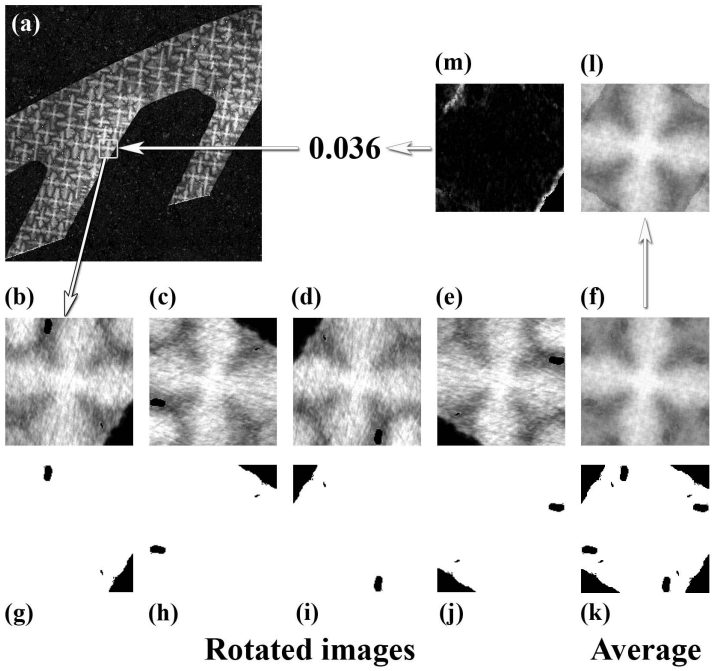

Figure 5: This schematic shows how a single pixel within the image is processed using the four-fold symmetry filter at a single length scale. A 300 x 300 μm neighborhood centered around a single pixel within (a) is chosen. Images (b)-(e) and (g)-(j) show the local image and its associated binary image (with mount and eutectic particles in black) for four 90° rotations. Images (f) and (g) are the average of the four rotated images. Image (l) corrects the average intensity for the mount material and eutectic particles, while image (m) shows the deviation between image (l) and image (b). The inverse of the sum of the values in image (m) is the four-fold symmetry value for the starting pixel.

mount material and eutectic particles are given an intensity value of zero in Figure 5(b).

2. The intensity image (Figure 5(b)) and binary image (Figure 5(g)) are rotated by 90° three times to produce the images shown in Figures 5(c)-5(e) and Figures 5(h)-5(j), respectively.
3. The four rotated images in Figures 5(b)-5(e) and Figures 5(g)-5(j) are averaged to generate Figures 5(f) and 5(g), respectively. This, however, does not account for the mount material or eutectic particles in the rotated images. Figure 5(l) corrects the average intensity by accounting for pixels where the mount material and eutectic particles have contributed.
4. Figure 5(m) shows an image of the squared deviation at every pixel between the intensity values in Figure 5(l) and Figure 5(b). Next, the values in Figure 5(m) are summed for all pixels which are not mount material or eutectic particles (i.e., all the white pixels in Figure 5(g)). The inverse of this value is the four-fold symmetry value for the single starting pixel (0.036).

Figure 6(a) shows an example of one of the serial slices after applying the four-fold symmetry filter technique outlined in Figure 5 with the subsequent post-processing filters (Gaussian, top hat filters) as described in Section 3.1. Figure 6(b) shows the original intensity image with the dendrite cores identified through a user-specified threshold parameter applied to Figure 6(a) (the red dots were enlarged slightly to show the dendrite core locations).

To assess the quality of this technique, the results of the automated symmetry-based technique were compared to the ground truth obtained from manual identification of the dendrite cores. The symmetry-based technique correctly

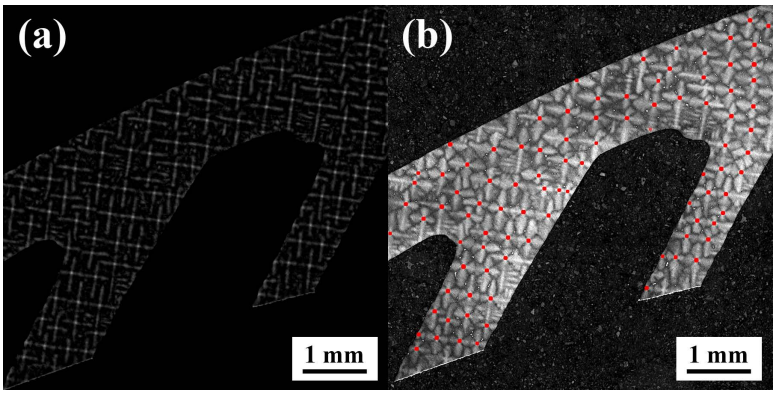

Figure 6: These images show an example of how the four-fold symmetry filter performs when applied to a 6-mm x 6-mm section of a serial slice. Figure 6(a) shows the vector-based final image and Figure 6(b) shows the original intensity image with the segmented dendrite cores (red) identified through a user-specified threshold parameter.

identified 92 dendrite core locations in this image with only 1 area incorrectly identified as a dendrite core (secondary dendrite arm intersecting a tertiary arm near the mount material). Additionally, there was one dendrite core in the interior that was missed, but should have been detected. Several dendrite cores at the mount material/microstructure boundary were not identified, but might have been identified manually depending on the operator. Overall, the results of the symmetry-based technique are good considering the difficulty of accounting for confounding features within the image. As can be observed from Figure 4(d), this technique does extremely well without these confounding features. The statistics from all 16 serial images show that, on average, 94 features were detected, of which 5.25 features were not dendrite cores (5.6%), and 6.31 dendrite cores were not detected (6.7%).

3.3. Improving Feature Extraction using Continuity Rules

The continuity of the dendritic cores from slice to slice can be exploited to improve extraction of dendrite core locations. A set of continuity rules may help locate missed dendrite cores and help discount incorrectly identified features. For instance, a dendrite core will typically appear on multiple slices. For missed dendrite cores, the adjacent slices may have detected dendrite cores, indicating that the missed dendrite core should probably be included. For incorrectly identified features, the adjacent slices may not have detected dendrite cores, indicating that the incorrectly identified feature is not a dendrite core.

An initial set of continuity rules was applied to the stack of 16 binary images generated using a manually-identified threshold parameter. First, the images obtained with the four-fold symmetry filter were aligned via rotation and translation using an autocorrelation technique[1]. Then, the binary images were generated by (i) manually selecting a threshold parameter to segment the four-fold symmetry image for each slice, and (ii) replacing each segmented object[2] with a circle with radius c_1. Then the following continuity rules were applied to improve the segmentation on individual binary images:

- **Rule 1 - Minimum dendrite length.** The dendritic core will have a minimum length in the $\langle 100 \rangle$ direction of c_2 or greater. Therefore, this rule eliminates objects that may only appear on a few adjacent slices, but not any slices before or afterwards.
- **Rule 2 - Minimum slice occurrence.** The dendritic cores appear on at least c_3 percent of the slices between the start and end of each dendrite. This rule eliminates objects that appear randomly over multiple slices spaced a distance c_2 or greater. This rule also adds dendrite cores to the

[1] It is important to note that this will align the stack of images with the dendrite cores, not the fiducial markers in the mount. Subsequent re-alignment by the fiducial markers may be required in a later step.

[2] The term "object" is used to refer to a segmented area that may or may not be an actual dendrite core.

binary serial images if they occur in a great enough frequency, assuming that they are bounded by the starting and ending slice of that particular dendrite core.

- **Rule 3 - Minimum size threshold.** The dendritic cores grow vertically with respect to the aligned binary images and, hence, the circular objects should align fairly well. In general, this rule removes small artifacts with a size below c_4 that appear at the mount/material boundary.

Applying these rules to a stack of serial images should eliminate most incorrectly segmented objects and add dendrite core locations to the slices where the four-fold symmetry filter generated a lower-intensity peak. To increase the accuracy of these rules, the operator may manually subtract segmented objects and add dendrite cores to establish a "ground truth" image every so many slices. For this stack of serial images, a "ground truth" image was generated for the first and last slice and the following parameters were used: $c_1 = 13$ pixels, $c_2 = 50$ μm, $c_3 = 25\%$, $c_4 = 400$ pixels. Figure 7 shows a visual depiction of the continuity rules used herein.

Figure 8 examines how these continuity rules combine image information from multiple slices to improve the dendrite core extraction. Figure 8(a) shows

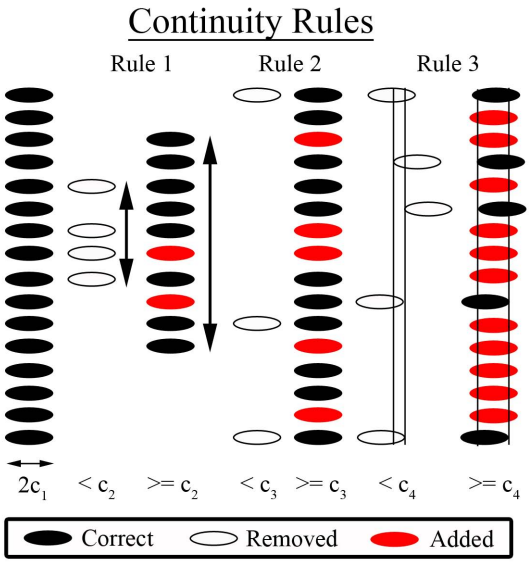

Figure 7: Schematic of the continuity rules used to augment identification of dendrite cores based on adjacent slice information. The identified dendrite cores are replaced by a circle of radius c_1 prior to executing the continuity rules. Rules 1, 2 and 3 refer to a minimum dendrite length (c_2), minimum dendrite occurrence (c_3), and minimum size threshold (c_4).

the segmented objects (black) from all 16 slices on one image. Figure 8(b) shows the 70 objects that appear on all 16 slices. Since all of these objects are dendrite cores, this subfigure indicates that the dendrite cores in the interior of the blade are the easiest to segment. Note that over 70% of the dendrite cores were easily segmented on all 16 slices. As was observed in Figure 4(d), images with a low density of confounding features should have higher dendrite core detection rates. Figure 8(c) shows the objects eliminated by the continuity rules. Almost all of the objects eliminated were at the mount/microstructure boundary, although a few were in regions where the dendrite growth direction changed. Three of the deleted objects are circled in red to show that these may have been manually identified as dendrite cores at the mount/microstructure boundary; these have also been circled in the image in Figure 8(d). Figure 8(d) shows the modified extraction of the dendrite core locations using the continuity rules. The four-fold symmetry filter with the continuity rules does an effective job of extracting most dendrite cores. The blue circles in this subfigure represent dendrite cores that should have been detected, but were not detected due to inadequate image pre-processing. The problem responsible for detecting these dendrite cores is shown in Figures 9(e)-9(h) and is discussed in Section 3.4.

3.4. Current Problems / Potential improvements

This symmetry-based technique can considerably reduce the amount of time spent manually identifying all dendrite cores within a serial image the size of Figure 1 or larger. However, at this point, this technique can still be improved. Several problems were encountered when using this technique to identify dendrite cores in a single crystal turbine blade. Figure 9 shows some examples where the current technique has problems and where modifications can lead to potential improvements. These are left for future work, but would be essential for fully automating this process to construct the 3D dendrite core structure.

Figures 9(a) and 9(c) show images on nearby slices, on which the dendrite core is detected on one and not on the other. Figures 9(b) and 9(d) show the complementary four-fold symmetry filtered images to Figures 9(a) and 9(c), where the maximum intensity in the dendrite cores was 54 and 50, respectively. However, in Figure 9(d), the white arrow points to a region with a higher intensity for this image (54), which would mean that an incorrect object would be identified prior to identifying the dendrite core at the boundary. Additionally, these subfigures illustrate the problem with identifying cores at the boundary at what point do the dendrite arms cease to have a core? In many cases, the intersection of the dendrite arms (the dendrite core) is right on the mount/microstructure boundary, or appears to be a little outside the boundary. While this is a problem with repeatability from slice to slice, modifying parameters within the continuity rules or adding new continuity rules may help to better identify dendrite cores at the boundaries.

The input image quality certainly affects the output of the four-fold symmetry technique. Improvements in the four-fold symmetry technique can be realized by reducing scratches and increasing intensity contrast within the serial intensity images through either experimental methodology or subsequent image processing

techniques. Additionally, this technique uses the segmented mount material and eutectic particles. Improving the segmentation of either of these features will improve the results presented in this article.

One example of how improving segmentation would improve the results is shown in Figures 9(e) and 9(g). This dendrite core lies near the mount/ microstructure boundary and was not identified on any of the slices with this technique. In both subfigures, the mount material and eutectic particles have been segmented and are indicated by black pixels. The difference between these figures is that in Figure 9(g), the segmented mount material was modified to remove the white pixels on the bottom edge of the microstructure (a remnant of the EDM fillet cut through the interior of the blade). The corresponding four-fold symmetry images are shown in Figure 9(f) and 9(h). The maximum

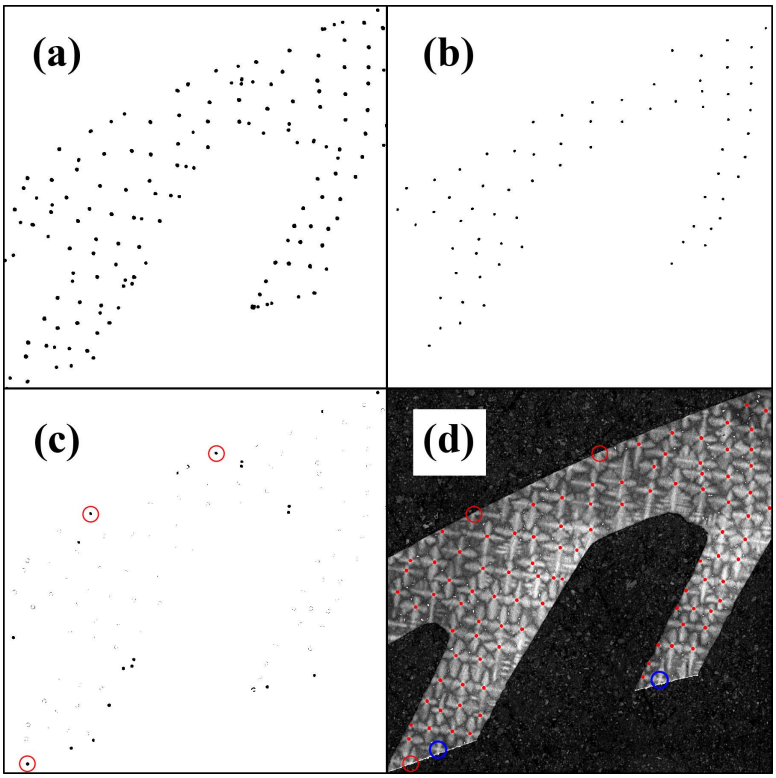

Figure 8: These images show the effect of applying continuity rules to combine image information from multiple slices. Figure 8(a) shows the segmented objects (black) from all 16 slices, Figure 8(b) shows the 70 objects that appear on all 16 slices, Figure 8(c) shows the objects eliminated by the continuity rules, and Figure 8(d) shows the modified extraction of the dendrite core locations using the continuity rules.

intensity value for the dendrite core was increased by 87% in Figure 9(h), assuring detection of the dendrite core.

Reducing the amount of time spent manually selecting a threshold parameter to segment the four-fold symmetry filtered serial images would also improve the current technique. A potential method for automating this is to establish a "ground truth" image for the first slice and then automate the selection of this threshold parameter on subsequent adjacent slices by optimizing a penalty function. This penalty function can be based on the number correctly identified and the number incorrectly identified. Once the penalty function for the adjacent slice is optimized, this segmentation can then be used to optimize segmentation on the next slice. In this manner, all slices after the first slice can be automatically segmented using a penalty function. An example of maximizing a penalty function (number of correct minus the number incorrect) to automate segmentation is shown in Figure 9(i), where 91 dendrite cores are correctly identified and 3 objects are false positives (circled in white).

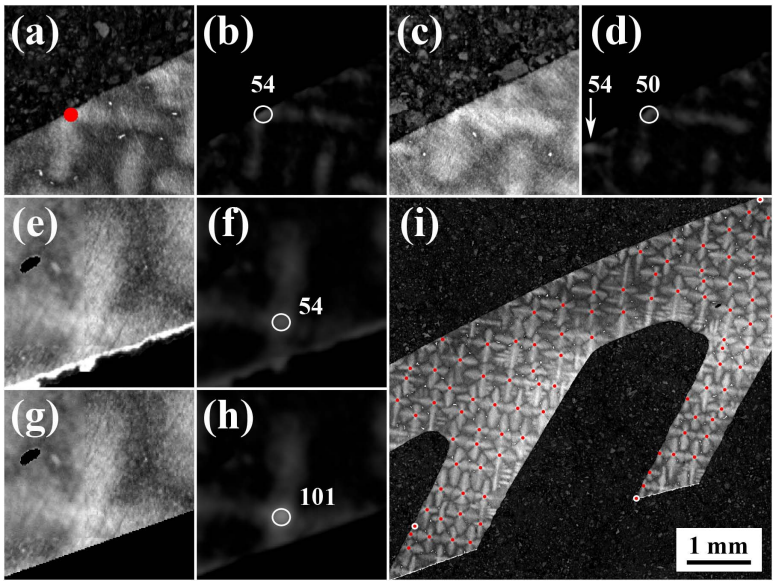

Figure 9: These images show examples of some problems as well as potential improvements to the current technique. Figures 9(a) and 9(c) show example images of dendrite cores at the mount/microstructure boundary and the difficulty with segmenting the dendrite core from the four-fold symmetry images (Figures 9(b) and 9(d), respectively). Figures 9(e) and 9(g) show how improving segmentation of the mount material can impact the four-fold symmetry value (in Figures 9(f) and 9(h), respectively). Figure 9(i) shows an example of automated selection of the threshold parameter for segmenting dendrite cores using a "ground truth" image from an adjacent slice.

Last, the four-fold symmetry filter is certainly a more computationally-intensive segmentation algorithm compared to more conventional methods. The computational time required increases with increasing neighborhood size. The more complex case which uses five local neighborhood sizes has been optimized for speed by first calculating a matrix containing the individual four-fold symmetry values for each pixel within the largest neighborhood size (e.g., Fig. 2(h)) and then using the relevant four-fold values from each neighborhood size to calculate the final four-fold symmetry for that pixel. Additional minor improvements to the algorithm performance can be made by only considering one quarter of the image for the summation operations in Fig. 2(f)-2(g) and then expanding this image for the final steps.

4. Conclusion

This article discusses an automated technique for extraction of the spatial locations of dendrite cores from serial images taken a production turbine blade composed of a heat-treated single crystal Ni-based superalloy. The technique incorporates image information over multiple length scales and exploits the four-fold symmetry of the dendrites when viewed down the $\langle 100 \rangle$ growth direction. Additional rules take advantage of the continuity of the dendrites from slice to slice to help exclude segmentation artifacts and improve dendrite core segmentation. The key results of this study are how to extract the locations of symmetric microstructural features in images by using the symmetry-based technique [28] augmented with information from adjacent slices and confounding image features (e.g., microstructure, eutectic particles). Automated techniques that operate on symmetric features can be a valuable tool for quantitatively characterizing material microstructures.

Acknowledgments

This work was performed at the Air Force Research Laboratory, Materials and Manufacturing Directorate, AFRL/RXLM, Wright-Patterson Air Force Base, OH. MAT would like to acknowledge the Center for Advanced Vehicular Systems (CAVS) at Mississippi State University for supporting this work.

References

[1] J.E. Spowart, Scripta Materialia 55 (2006) 5-10.
[2] J.E. Spowart, H.M. Mullens, B.T. Pachula, JOM 55(10) (2003) 35-37.
[3] J. Alkemper, P.W. Voorhees, Journal of Microscopy 201 (2001) 388-394.
[4] M.D. Uchic, M. De Graef, R. Wheeler, D.M. Dimiduk, Ultramicroscopy, in press.
[5] Groeber, Ghosh, Haley, Uchic, Dimiduk, Materials Characterization 57 (2006) 259-273.

[6] W. Xu, M. Ferry, N. Mateescu, J.M. Cairney, F.J. Humphreys, Materials Characterization 58 (2007) 961-967.
[7] W. Xu, M. Ferry, J.M. Cairney, F.J. Humphreys, Acta Materialia 55 (2007) 5157-5167.
[8] B.J. Inkson, M. Mulvihill, G. Mobus, Scripta Materialia 45 (2001) 753-758.
[9] J. Madison, J.E. Spowart, D.J. Rowenhorst, T.M. Pollock, JOM July (2008) 26-30.
[10] J. Madison, J.E. Spowart, D.J. Rowenhorst, J. Fiedler, T.M. Pollock, Superalloys Conference Proceedings (2008) 881-888.
[11] J.L. Fife, P.W. Voorhees, Acta Materialia 57 (2009) 2418-2428.
[12] R. Mendoza, J. Alkemper, P.W. Voorhees, Metallurgical and Materials Transactions A 34 (2003) 481-489.
[13] D. Kammer, P.W. Voorhees, Acta Materialia 54 (2006) 1549-1558.
[14] D. Kammer, R. Mendoza, P.W. Voorhees, Scripta Materialia 55 (2006) 17-22.
[15] M. Li, S. Ghosh, T.N. Rouns, H. Weiland, O. Richmond, W. Hunt, Materials Characterization 41 (1998) 81-95.
[16] M. Li, S. Ghosh, O. Richmond, H. Weiland, T.N. Rouns, MSE 265 (1999) 153-173.
[17] M.V. Kral, G. Spanos, Acta Materialia 47 (1999) 711-724.
[18] M.V. Kral, M.A. Mangan, G. Spanos, R.O. Rosenberg, Materials Characterization 45 (2000) 17-23.
[19] A.C. Lewis, J.F. Bingert, D.J. Rowenhorst, A. Gupta, A.B. Geltmacher, G. Spanos, MSE 418 (2006) 11-18.
[20] D.J. Rowenhorst, A. Gupta, C.R. Feng, G. Spanos, Scripta Materialia 55 (2006) 11-16.
[21] B. Maruyama, J.E. Spowart, D.J. Hooper, H.M. Mullens, A.M. Druma, C. Druma, et al., Scripta Materialia 54 (2006) 1709-1713.
[22] A.C. Lund, P.W. Voorhees, Philosophical Magazine 83 (2003) 1719-1733.
[23] A.C. Lund, P.W. Voorhees, Acta Materialia 50 (2002) 2085-2098.
[24] R.S. Sidhu, N. Chawla, Materials Characterization 52 (2004) 225-230.
[25] S.G. Lee, A.M. Gokhale, A. Sreeranganathan, MSE A 427 (2006) 92-98.
[26] M.A. Tschopp, M.A. Groeber, R. Fahringer, J.P. Simmons, A.H. Rosenberger, C. Woodward, MSMSE, 18 (2010) 025014.
[27] S. Ghosh, J. Bai, P. Raghavan, Mechanics of Materials 39 (2007) 241-266.
[28] M.A. Tschopp, M.A. Groeber, R. Fahringer, J.P. Simmons, A.H. Rosenberger, C. Woodward, Scripta Materialia, 62 (2010) 357-360.
[29] M. Groeber, R. Farringer, D. Dimiduk, C. Woodward, et al., to be submitted.
[30] Russ, J.C., The Image Processing Handbook, 5th Edition (Boca Raton, FL, CRC Press, 2007).
[31] Gonzalez, R.C., Woods, R.E., Digital Image Processing, 2nd Edition (Upper Saddle River, NJ, Prentice-Hall, 2002).

[32] Tschopp, M.A., Tiley, J.S., Viswanathan, G.B., Materials Science & Technology, in press, doi:10.1179/026708309X12560332736638.

[33] J.P. Simmons, P. Chuang, M.L. Comer, M. Uchic, J.E. Spowart, M. De Graef, MSMSE 17 (2009) 025002.

[34] E.B. Gulsoy, M. De Graef, Microscopy & MicroAnalysis, 15(S2) (2009) 606CD.